Supplementary Material for: Strong coupling between mechanical modes in a nanotube resonator

A. Eichler[1], M. del Álamo Ruiz[1], J. A. Plaza[2], and A. Bachtold[1]

[1]*Institut Català de Nanotecnologia, Campus de la UAB, E-08193 Bellaterra, Spain and*

[2]*IMB-CNM (CSIC), E-08193 Bellaterra, Barcelona, Spain*

I. DEVICE FABRICATION

Our nanoresonators consist of a suspended carbon nanotube clamped between two metal electrodes, as depicted in Fig. 1(a) and (b) of the main text. The devices are fabricated as follows. A trench is etched into a highly resistive Si wafer coated with SiO_2 and Si_3N_4. W and Pt are evaporated into the trench to create a gate electrode (G). In a second lithography step, a continuous line is exposed across the trench. After a deposition of W/Pt and lift-off, the line results in the source (S) and drain (D) electrodes separated by the trench (these electrodes are electrically isolated from the gate due to the undercut profile of the Si_3N_4/SiO_2 substrate). W and Pt are chosen because of their high melting points that allow the growth of carbon nanotubes. An island of catalyst is patterned on the drain (or source) electrode using electron-beam lithography. Nanotubes are grown by chemical vapour deposition from these islands. In about 1 out of 20 cases, a nanotube grows across the trench and establishes electrical contact between S and D. This growth is the last step of the fabrication process so that nanotubes are not contaminated with residues from resists and chemicals [1–3]. The device we present in the main text has a length of 1.77 μm. The separation between the nanotube and the gate electrode is 370 nm. The rather large roughness of the S and D electrodes in this device does not allow us to measure the nanotube radius with atomic force microscopy.

II. MEASUREMENTS DETAILS

Our measurements are carried out at pressures typically below 10^{-8} mbar and temperatures between 60 and 70 K. In order to clean the nanotube surface, we perform a current annealing step every day (6 μA for 300 s). We observe only very minor variations of the electrical conductance and mechanical resonance frequencies of the nanotube from day to day.

The chip containing the device is mounted on a printed circuit board. dc and ac voltages are added through a bias tee outside the chamber. The low frequency mixing current is measured from the drain (D) electrode and is low-pass filtered through a capacitor to ground (1 nF).

We discuss first the frequency mixing (FM) technique [4]. A driving voltage V^{ac} is applied to the source electrode. Modulating the frequency (with a modulation rate of 671 Hz and a frequency deviation of 100 kHz) results in a mixing current (I_{mix}) at 671 Hz. The gate electrode is biased with a dc voltage V_g to tune the resonance frequencies.

In the two-source technique [5], we apply the driving voltage V^{ac} to the gate in addition to a dc voltage V_g. The motion of the nanotube is detected by applying a second, smaller voltage V_s^{ac} to the source. The two oscillating voltages are slightly detuned, and the amplitude signal of I_{mix} is measured at the detuning frequency ($\delta\omega/2\pi = 10\,\mathrm{kHz}$).

The modulus of I_{mix} measured with the two-source technique has the form

$$I_{mix} = \frac{1}{2} V_s^{ac} \frac{\partial G}{\partial V_g} \left(V^{ac} \cos(\delta\omega t - \varphi_E) + z_0 V_g \frac{C'}{C} \cos(\delta\omega t - \varphi_E - \varphi_M) \right) \tag{S1}$$

where G is the conductance of the nanotube, φ_E is the phase difference between the voltages applied to source and gate, t is time, z_0 is the mechanical amplitude, C is the capacitance between the nanotube and the gate, C' is its derivation with respect to the nanotube displacement, and φ_M is the phase difference between the nanotube displacement and the driving force.

The measurements in the paper of I_{mix} as a function of the drive frequency f give a resonance lineshape that is to a rather good approximation proportional to the response of the motional amplitude as a function of f, since the purely electrical component of I_{mix} (first term in Eq. S1) is much lower than the mechanical component (second term in Eq. S1).

We verify that the harmonics of the RF sources (signals at 2, 3, or 1/2 times the drive frequency) can be neglected. These harmonics are far below the smallest driving voltage for which we can detect a resonance. Namely, the voltage of the harmonics is typically 1000 times lower than V^{ac}.

III. ESTIMATION OF DYNAMICAL AMPLITUDE

Equation S1 allows estimating the motional amplitude of the resonator by comparing the signal on resonance, I_{max}, to the purely electrical background far from resonance, I_{back} [5]. Using the approximation $C = \frac{2\pi\epsilon_0 L}{\ln(2(d-z)/r)}$, we get that

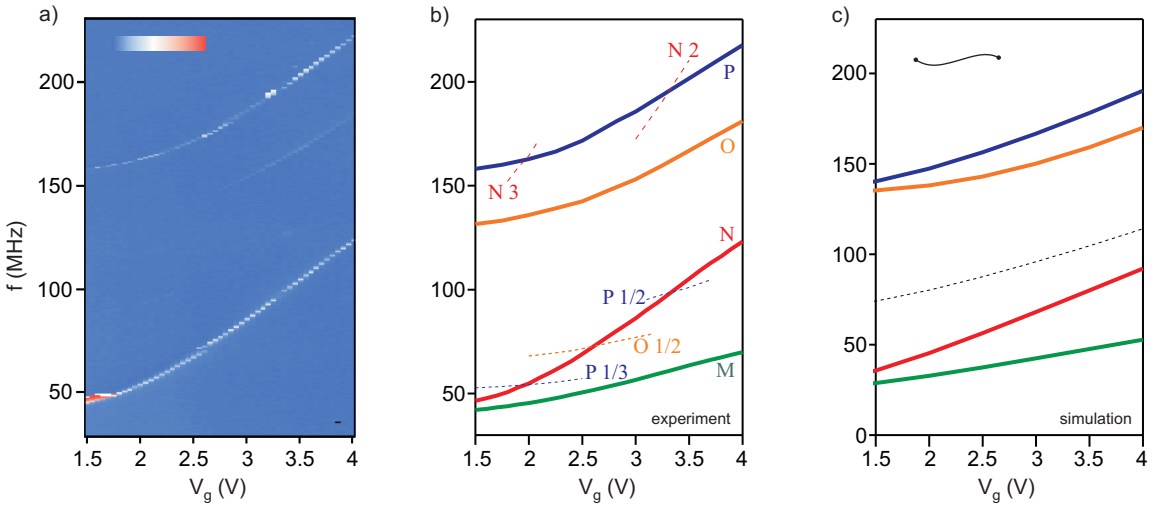

FIG. S1: Maps of resonance frequencies as a function of gate voltage. (a) Two-source measurement at low driving force (obtained by measuring I_{mix} as a function of f and V_g with $V^{ac} = 1.7\,\mathrm{mV}$ and $V_s^{ac} = 0.3\,\mathrm{mV}$). Colour scale: 0 (blue) to 1 nA (red). For comparison, we plot the schematic of the modes detected with the FM technique in (b) and the results of the ANSYS simulation in (c). The inset in (c) shows the static nanotube shape (measured in the absence of an applied dc voltage) that is used in the simulation.

$$z_0 \simeq d \cdot \ln\left(\frac{2d}{r}\right) \frac{I_{max}}{I_{back}} \frac{V^{ac}}{V_g} \tag{S2}$$

with $d = 370\,\mathrm{nm}$ the equilibrium distance between the nanotube and the gate electrode. Since we cannot measure the diameter of the nanotube due to the large surface roughness of the electrodes in the studied device, we use a typical value for the radius ($r = 1.5\,\mathrm{nm}$). We find the following values for the maximum mechanical amplitudes z_0 in Fig. 1 of the main text: $z_0 \simeq 3.2\,\mathrm{nm}$ in Fig. 1(c), $z_0 \simeq 8.7\,\mathrm{nm}$ in Fig. 1(d), $z_0 \simeq 0.9\,\mathrm{nm}$ in Fig. 1(e), and $z_0 \simeq 2.1\,\mathrm{nm}$ in Fig. 1(f).

IV. MAPS OF RESONANCE FREQUENCIES AS A FUNCTION OF GATE VOLTAGE: COMPARISON BETWEEN THE TWO-SOURCE AND THE FM TECHNIQUES AT LOW DRIVING FORCES

We carry out measurements of the resonance frequencies as a function of V_g with the two-source technique at low driving force [Fig. S1(a)]. Two modes are detected with a large signal, a third

one with a small signal. To facilitate a comparison between the two measurement techniques, we plot the schematic of the modes detected with the FM technique in Fig. S1(b). We find that the modes producing a large signal with the two-source technique are those we label N and P. The mode producing a weak signal is identified as O, while M is not detected at all (it does show up at larger driving forces).

The ANSYS simulation helps understanding the relative strengths of the signals [Fig. S1(c)]. The details of the simulation are discussed in section VII. N and P correspond to modes moving essentially in the plane orthogonal to the gate electrode. Since the two-source method measures the oscillation of the nanotube-gate capacitance, the signal of modes N and P are expected to be large, in agreement with the experiments. M and O are modes moving essentially parallel to the gate electrode. As such, the corresponding signals are expected to be small, which also agrees with the measurement.

ANSYS simulations indicate that modes M, N, O, and P have either 0 or 2 nodes. The mode with 1 node moving perpendicular to the gate electrode is predicted to appear between N and O [dashed line in Fig. S1(c)]. This mode is not detected because the oscillation of the capacitance is (nearly) zero due to the symmetry of the mode shape. ANSYS predicts that the mode with 1 node parallel to the gate has a frequency larger than that of modes O and P.

V. MAPS OF RESONANCE FREQUENCIES AS A FUNCTION OF GATE VOLTAGE: COMPARISON BETWEEN LOW AND HIGH DRIVING FORCES

In the maps of resonances as a function of V_g the number of detected resonances depends on the driving force F_d. Figure S2(a) shows the spectrum obtained with the two-source method for a low driving force. Upon increasing F_d by a factor 10, many more resonances appear Fig. S2‘(b)]. A comparison of the resonance frequencies reveals that the additional resonances are almost all harmonics of the four modes M, N, O, and P (see following section).

The same scenario develops for measurements with the FM technique at high driving force: additional resonances are detected [Fig. S3(a) and (b)] and identified as harmonics of the four modes (see following section). Here, the number of discernible harmonics is even larger than that measured with the two-source technique.

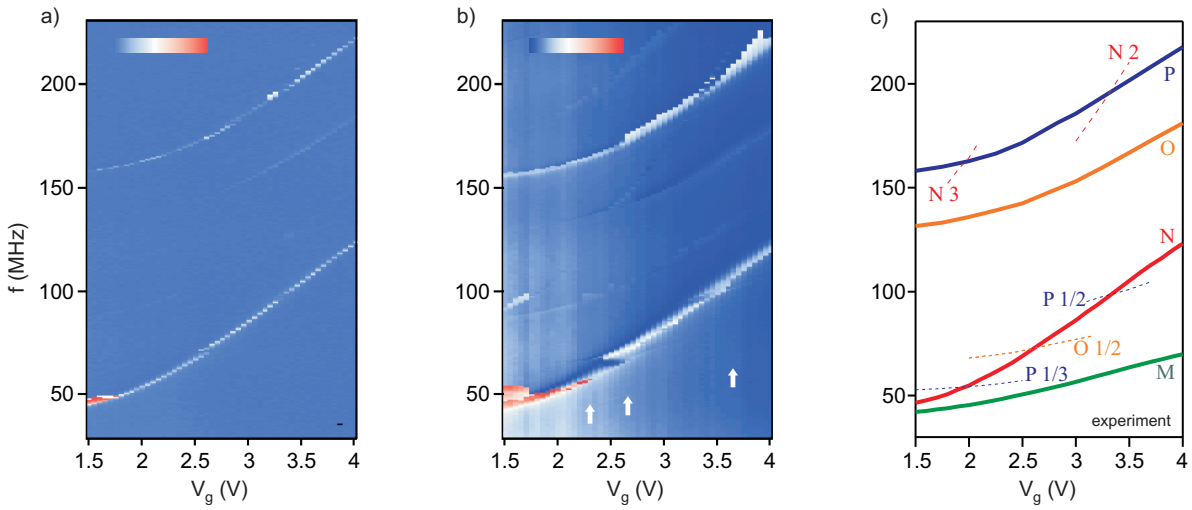

FIG. S2: Map of resonance frequencies as a function of gate voltage. (a) Two-source measurement at low driving force (obtained by measuring I_{mix} as a function of f and V_g with $V^{ac} = 1.7\,\mathrm{mV}$ and $V_s^{ac} = 0.3\,\mathrm{mV}$). Colour scale: 0 (blue) to 1 nA (red). (b) Same measurement with a larger driving force ($V^{ac} = 17\,\mathrm{mV}$ and $V_s^{ac} = 1.1\,\mathrm{mV}$). White arrows point out the lowest mode which is faintly visible. Colour scale: 0 (blue) to 7 nA (red). (c) Schematic of the modes detected with the FM technique for comparison.

VI. HARMONICS

In Fig. S4, we plot the four modes and their harmonics on top of each other by dividing each of them by their respective harmonic order [i.e. the index number in Fig. S3(c)]. In the case of the modes N, O, and P, the curves are perfectly on top of each other. For mode M, the scaling is slightly less good. Harmonics can be generated by several mechanisms. In the following, we will briefly discuss the parametric effect, electrical nonlinearities, and mechanical nonlinearities as possible origin of the harmonics.

A common way to explain harmonics is based on the parametric effect [6, 7]. A mode at a resonance frequency f_0 can be actuated by varying the resonator spring constant k at a frequency $2f_0/j$, where j is an integer ≥ 1. It is easy to parametrically drive a nanotube resonator with a gate voltage, because f_0 (and therefore k) is widely tunable with V_g [8]. There exists a threshold V_{th}^{ac} above which the motion sets in: this threshold takes the form $V_{th}^{ac} = (f_0 \partial V_g/\partial f_0)/Q$, where $\partial f_0/\partial V_g$ is the change of the resonance frequency with gate voltage. For mode N, we get $\partial f_0/\partial V_g =$

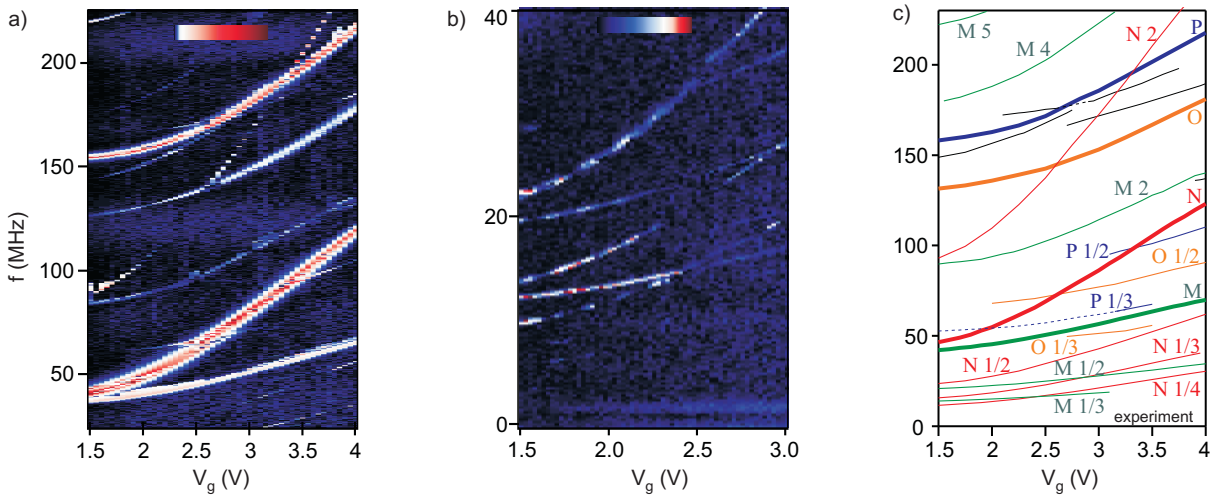

FIG. S3: Map of resonance frequencies as a function of gate voltage measured with the FM technique. (a) Frequency modulation measurement at large driving force (obtained by measuring I_{mix} as a function of f and V_g with $V^{ac} = 20\,\mathrm{mV}$). Colour scale: 0 (black) to 1 nA (dark red). (b) Low frequency range at even higher driving force ($V^{ac} = 40\,\mathrm{mV}$). Colour scale: 0 (black) to 0.2 nA (dark red). (c) Map of all detected modes and harmonics. The number in the label designates the harmonic order of a resonance. Black lines correspond to resonances that cannot be assigned to a detected mode.

36 MHz/V close to $V_g = 4\,\mathrm{V}$. Together with the quality factor $Q \sim 350$ and $f_0 \sim 124\,\mathrm{MHz}$, this yields a threshold of 10 mV. This is consistent with the harmonics for mode N in Fig. S3(a) ($V^{ac} = 20\,\mathrm{mV}$). However, parametric excitation cannot account for the harmonics of order 4 and 5 of mode M.

A second scenario for harmonics is related to electrical nonlinearities in the circuit. Nonlinearities in current-voltage characteristics can generate forces at 2, 3, 4,... times the frequency of the applied V^{ac} and thus lead to harmonics with an index number $n < 1$. However, harmonics with an index number $n > 1$ are unlikely to have an electrical origin.

Mechanical nonlinearities are predicted to give rise to harmonics. For instance, the quadratic nonlinear force can cause harmonics at $2f_0$ and $f_0/2$, and the cubic nonlinear force can induce harmonics at $3f_0$ and $f_0/3$ [6, 9]. The combination of the quadratic and the cubic nonlinear forces can lead to harmonics with index 1/2, 1/3, 1/4, 2, 3, 2/3, 3/2,... [6], which is in agreement with our measurements.

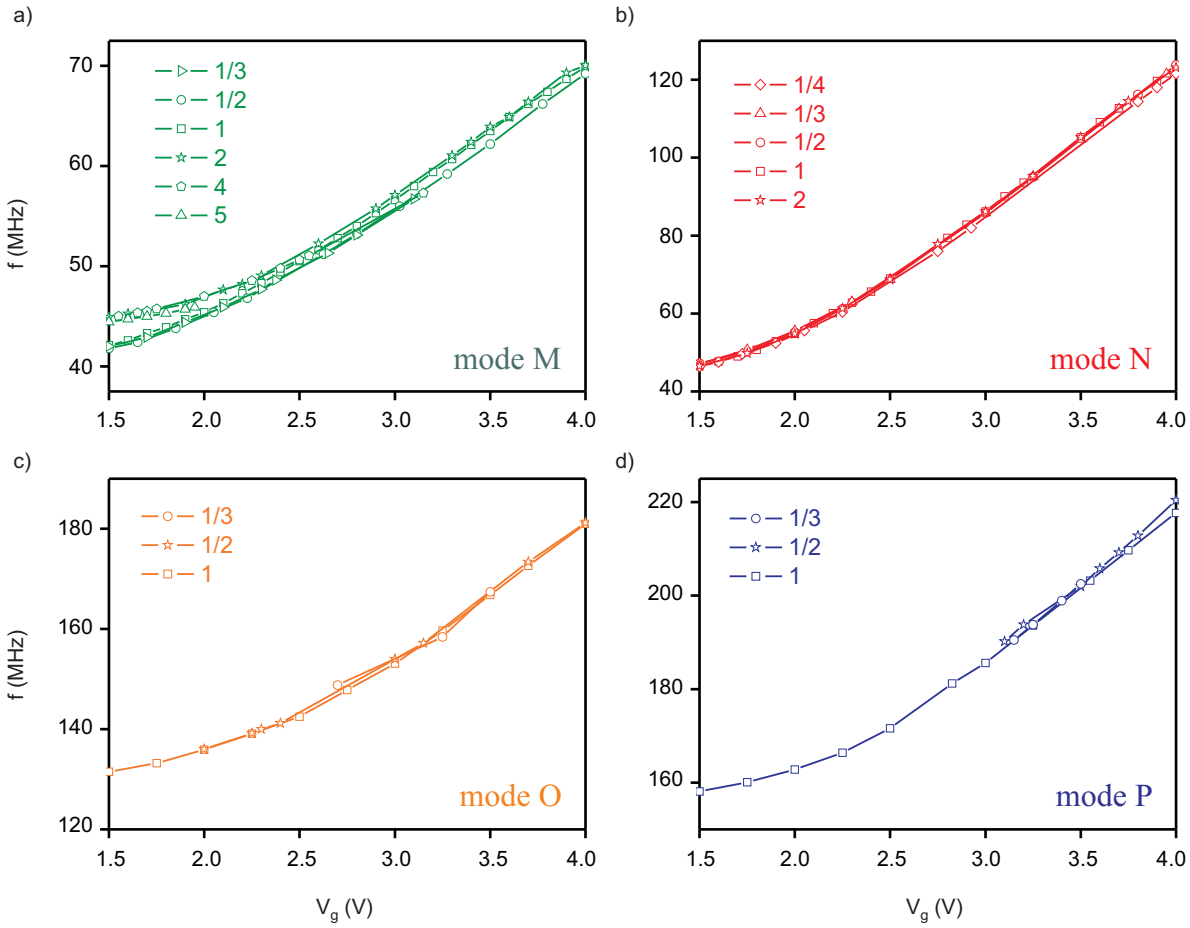

FIG. S4: Comparison of the modes with their harmonics. Each harmonic is divided by its respective order [corresponding to the index in Fig. S3(c)]. (a) Mode M and harmonics. The subharmonics ($M2$, $M4$, and $M5$) deviate slightly at low values of V_g. (b) Mode N and harmonics. (c) Mode O and harmonics. (d) Mode P and harmonics.

In conclusion, the origin of the harmonics is not clear at the moment and this calls for future work.

VII. SIMULATIONS

We perform finite element simulations with ANSYS (R) Release 13.0 to reproduce the V_g dependence of the resonance frequencies. The mechanical properties of carbon nanotubes are well described by continuum elasticity and are independent of the chirality [10]. For these simulations,

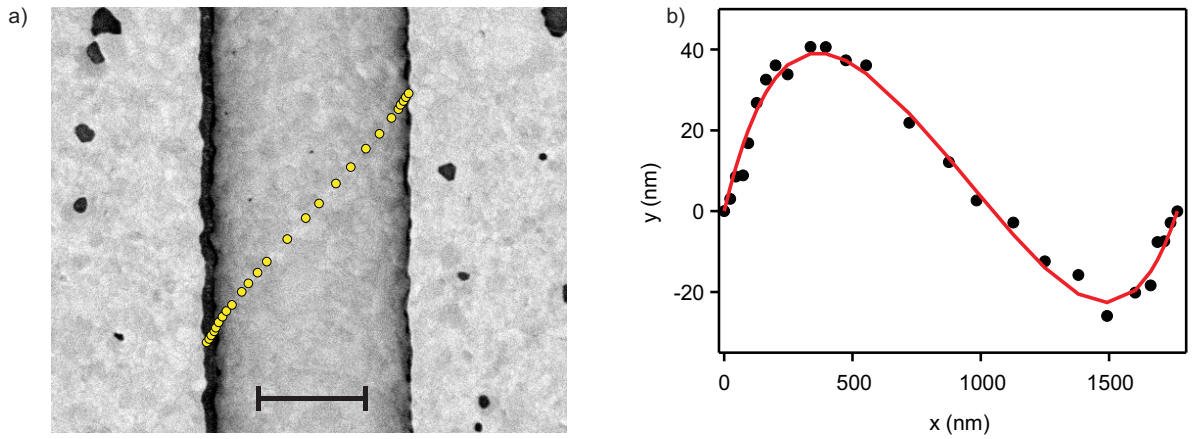

FIG. S5: Static shape of the nanotube. (a) Scanning electron micrograph of the nanotube. The electrodes are not voltage biased. Yellow dots mark the data points that we used to model the nanotube shape (for $V_g = 0\,\mathrm{V}$). Scale bar: 600 nm. (b) Points extracted from the electron micrograph (black dots) and polynomial fit used for the nanotube model (red line). x is the coordinate along the axis connecting the two clamping points. y is the coordinate standing orthogonal to it.

we use a tube with length $L = 1.77\,\mu\mathrm{m}$, radius $r = 1.5\,\mathrm{nm}$, wall thickness $\Delta r = 0.335\,\mathrm{nm}$, mass density $\rho = 2300\,\mathrm{kg/m^3}$, and Young modulus $E = 1\,\mathrm{TPa}$. We use the shape of the nanotube extracted from the scanning electron micrograph of the device (Fig. S5). We assume that the static deformation is only in the horizontal plane when the device is not voltage biased.

We use the 1-D BEAM188 element suitable for analyzing slender beam structures. 1-D BEAM188 is a two-node element in 3-D and has six degrees of freedom at each node: translations in the x, y, and z directions and rotations about the x, y, and z directions. A circular tube section is associated to the element by providing the inner and the outer radii. The constraints at the clamping points are fixed by setting all degrees of freedom to zero. Because of the high aspect ratio of nanotubes, we use point-like clamping conditions. The effect of the angle of the nanotube with respect to the electrodes is thus not accounted for. The electrostatic force induced by the dc voltage applied on the gate electrode, F_d, is analytically calculated. For each gate voltage, the static deformation of the nanotube is calculated by performing a nonlinear structural analysis. This static solution is used as a base for the modal analysis.

VIII. EULER-BERNOULLI EQUATION: MODE FREQUENCIES

In the following, we demonstrate that a good qualitative understanding of the motion of a suspended nanotube is possible from the Euler-Bernoulli equation. This approach provides analytical solutions that capture the behaviour of the system and that are similar to the solutions of the finite-element simulations performed with ANSYS.

The Euler-Bernoulli equation for the static and dynamic displacement of a thin beam reads

$$\rho S \frac{d^2 z}{dt^2} = -EI \frac{d^4 z}{dx^4} + \left[T_0 + \frac{ES}{2L} \int_0^L \left(\frac{dz}{dx} \right)^2 dx \right] \frac{d^2 z}{dx^2} + g(t) \tag{S3}$$

where ρ is the mass density, S the beam's cross-sectional area, z the displacement, t the time, E the Young modulus, I the second moment of inertia about the longitudinal axis, x the coordinate along the axis, T_0 the built-in tension, L the resonator length, and $g(t)$ a unit length force that accounts for the effect of the gate electrode in our experiment. We divide the displacement into a static and a dynamic component,

$$z(x,t) = z_s \phi_s(x) + z_1(t) \phi_1(x) \tag{S4}$$

where z_s is the maximum static displacement, z_1 is the maximum dynamic displacement, and $\phi_s(x)$, $\phi_1(x)$ are the normalized static and dynamic profiles along the beam.

In a first example, we develop Eq. S3 for the case of a single mechanical mode with

$$\phi_s(x) = \phi_1(x) = \sin(\pi x / L) \tag{S5}$$

where both the static and dynamic profiles are in the plane perpendicular to the gate electrode. This mode profile is strictly correct for negligible bending rigidity ($EI \to 0$). We choose this ansatz because it allows a simple analytical treatment of our problem. Moreover, we will see at the end of this section that this ansatz predicts gate voltage dependencies of the resonance frequencies that are in qualitative agreement with finite element simulations. We insert Eq. S4 and Eq. S5 into Eq. S3, multiply Eq. S3 by $\phi_1(x)$, and integrate it from 0 to L to get

$$\frac{d^2 z_1(t)}{dt^2} = -\frac{1}{\rho S}\left[EIz_s\left(\frac{\pi}{L}\right)^4 + T_0 z_s\left(\frac{\pi}{L}\right)^2 + \frac{ES}{4}z_s^3\left(\frac{\pi}{L}\right)^4 - \frac{4}{\pi}g(t)\right] - \frac{1}{\rho S}\left[EI\left(\frac{\pi}{L}\right)^4 + T_0\left(\frac{\pi}{L}\right)^2 + \frac{3}{4}ESz_s^2\left(\frac{\pi}{L}\right)^4\right] z_1(t) - \left[\frac{3E}{4\rho}z_s\left(\frac{\pi}{L}\right)^4\right] z_1^2(t) - \left[\frac{E}{4\rho}\left(\frac{\pi}{L}\right)^4\right] z_1^3(t). \quad \text{(S6)}$$

In a static equilibrium position, the sum of the static terms in the first bracket on the right hand side of Eq. S6 is zero:

$$EIz_s\left(\frac{\pi}{L}\right)^4 + T_0 z_s\left(\frac{\pi}{L}\right)^2 + \frac{ES}{4}z_s^3\left(\frac{\pi}{L}\right)^4 = \frac{4}{\pi}g(t). \quad \text{(S7)}$$

The other terms of Eq. S6 can be rewritten in the usual form of a Newton equation of motion,

$$\frac{d^2 z_1(t)}{dt^2} = -\omega_0^2 z_1(t) - \alpha_2 z_1^2(t) - \alpha_3 z_1^3(t). \quad \text{(S8)}$$

From a comparison of Eq. S6 to Eq. S8, we see that both α_2 and α_3 are positive, and that $\alpha_2 \propto z_s$ (meaning that α_2 will vanish if the tube is straight). Further, both nonlinear coefficients are inversely proportional to L^4 and will become large for a short tube. They arise from additional tension that is generated when the beam bends (the integral term $\int_0^L \left(\frac{dz}{dx}\right)^2 dx$ in Eq. S3 becomes nonzero).

We repeat this calculation for other modes. The profile of the second mode, $\phi_2(x)$, has the same shape as $\phi_1(x)$, but stands orthogonal to it, moving parallel to the gate electrode. In this case, the final equation describing the second mode is somewhat simpler than that for the first mode:

$$\frac{d^2 z_2(t)}{dt^2} = -\frac{1}{\rho S}\left[EI\left(\frac{\pi}{L}\right)^4 + T_0\left(\frac{\pi}{L}\right)^2 + \frac{ES}{4}z_s^2\left(\frac{\pi}{L}\right)^4\right] z_2(t) - \left[\frac{E}{4\rho}\left(\frac{\pi}{L}\right)^4\right] z_2^3(t). \quad \text{(S9)}$$

Again, α_3 is positive, but here $\alpha_2 = 0$ because the beam features no static bending in the direction of its vibrations. The linear restoring force of $z_1(t)$ is always larger than that of $z_2(t)$, causing $\omega_1 \geq \omega_2$.

We assume that the third and fourth modes have the profile

$$\phi_3(x) = \phi_4(x) = \sin(2\pi x/L), \quad \text{(S10)}$$

moving towards and parallel to the gate electrode, respectively. The resonance frequencies of the two modes are degenerate. Neither of these modes are detected in our experiment due to the antisymmetrical mode profile. The solution in this case reads (with $i = 3$ or 4)

$$\frac{d^2 z_i(t)}{dt^2} = -\frac{1}{\rho S}\left[EI\left(\frac{2\pi}{L}\right)^4 + T_0\left(\frac{2\pi}{L}\right)^2 + \frac{ES}{16}z_s^2\left(\frac{2\pi}{L}\right)^4\right] z_i(t) - \left[\frac{E}{4\rho}\left(\frac{2\pi}{L}\right)^4\right] z_i^3(t). \quad \text{(S11)}$$

We assume that the fifth and sixth modes are analogous to the third and fourth, but with

$$\phi_5(x) = \phi_6(x) = \sin(3\pi x/L). \quad \text{(S12)}$$

Again, they are degenerate. We get (with $j = 5$ or 6)

$$\frac{d^2 z_j(t)}{dt^2} = -\frac{1}{\rho S}\left[EI\left(\frac{3\pi}{L}\right)^4 + T_0\left(\frac{3\pi}{L}\right)^2 + \frac{ES}{36}z_s^2\left(\frac{3\pi}{L}\right)^4\right] z_j(t) - \left[\frac{E}{4\rho}\left(\frac{3\pi}{L}\right)^4\right] z_j^3(t). \quad \text{(S13)}$$

At this point, we can calculate the resonance frequencies of the first six modes as a function of V_g. For this, we determine the static displacement that provides an equilibrium of forces by solving Eq. S7, where

$$g(t) = \frac{1}{2}c' V_g^2 \quad \text{(S14)}$$

is the unit length force due to V_g, and

$$c' = \frac{2\pi\varepsilon_0}{d\ln(2d/r)^2} \quad \text{(S15)}$$

is the differentiation of the unit length capacitance with respect to the displacement. Here, d is the distance between the nanotube and the gate electrode, $\varepsilon_0 = 8.85 \cdot 10^{-12}\,\mathrm{F m^{-1}}$ is the electrical permittivity of free space, and r is the nanotube radius. We measure $d = 370\,\mathrm{nm}$ by atomic force microscopy (AFM), but the large surface roughness of the electrodes of this device does not allow the measurement of r. We therefore chose a typical value from earlier nanotubes grown by the same method ($r = 1.5\,\mathrm{nm}$). We also use $E = 1\,\mathrm{TPa}$, $\rho = 2300\,\mathrm{kg/m}$ [11], $L = 1.77\,\mu\mathrm{m}$ (measured by AFM), and wall thickness $\Delta r = 0.335\,\mathrm{nm}$. From these values, we calculate the second moment of inertia $I = 2.928 \cdot 10^{-38}\,\mathrm{kg\,m^2}$ and the tubular cross-section $S = \pi((r+\Delta r)^2 - (r-\Delta r)^2) = 3.157 \cdot 10^{-18}\,\mathrm{m^2}$. The only free parameter, T_0, is chosen by optimizing the agreement of the mode

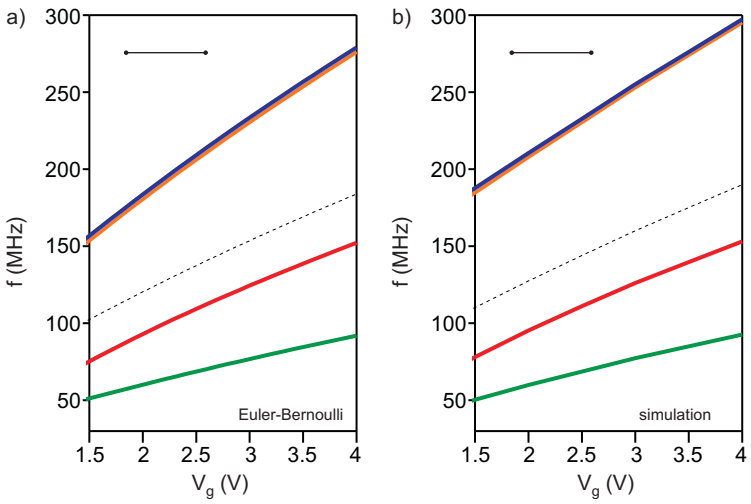

FIG. S6: Calculation of resonance frequencies as a function of V_g for a straight nanotube. (a) Resonance frequencies of the first six modes calculated from the Euler-Bernoulli equation. red: z_1, green: z_2, black dashed: z_3 and z_4 (not detected in our experiment due to the antisymmetrical mode profile), blue: z_5, orange: z_6. Inset: shape of the nanotube when $V_g = 0\,\mathrm{V}$. (b) ANSYS simulation for the same set of parameters. The results are very similar to the analytical calculations.

frequencies to the experimental results. We obtain $T_0 = 0.1\,\mathrm{nN}$. The resulting z_s as a function of V_g is shown in Fig. 2(e) of the main text. Finite element calculations with a straight tube yield values of z_s close to the results of Eq. S7, see dashed line in Fig. 2(e) of the main text. The resonance frequencies of the six first modes are depicted in Fig. S6(a).

IX. EULER-BERNOULLI EQUATION: COUPLING BETWEEN MODES

In the previous section, we have disregarded terms that couple different modes. The coupling has the same origin as the quadratic and cubic nonlinearities (α_2 and α_3). It arises from the tension that is induced in a mode when another mode oscillates (through the integral term $\int_0^L \left(\frac{dz}{dx}\right)^2 dx$ in Eq. S3). As a consequence, the coupling coefficients are of the same order of magnitude as α_2 and α_3. Assuming that $z(x,t) = z_s\phi_s(x) + z_1\phi_1(x) + z_2\phi_2(x)$, Eq. S3 leads to

$$\frac{d^2 z_1(t)}{dt^2} = -\omega_0^2 z_1(t) - \alpha_2 z_1^2(t) - \alpha_3 z_1^3(t) - \beta_{22} z_2^2(t) - \epsilon_{122} z_1(t) z_2^2(t) \tag{S16}$$

where ω_0, α_2, and α_3 are given by the expressions in Eq. S6, $\beta_{22} = \frac{E}{4\rho}\left(\frac{\pi}{L}\right)^4 z_s$, and $\epsilon_{122} = \frac{E}{4\rho}\left(\frac{\pi}{L}\right)^4$

(all other summands β_{jk} and ϵ_{jkl} that appear in Eq. 1 of the main text are zero). The equation of motion for the lowest mode moving parallel to the gate electrode is

$$\frac{d^2 z_2(t)}{dt^2} = -\omega_0^2 z_2(t) - \alpha_3 z_2^3(t) - \beta_{12} z_1(t) z_2(t) - \epsilon_{112} z_2(t) z_1^2(t) \tag{S17}$$

where ω_0 and α_3 are given by Eq. S9 and the coupling coefficients are $\beta_{12} = \frac{E}{2\rho}\left(\frac{\pi}{L}\right)^4 z_s$ and $\epsilon_{112} = \frac{E}{4\rho}\left(\frac{\pi}{L}\right)^4$.

X. ONSET OF NONLINEARITY

Nonlinear effects set in when z_0 reaches a critical value z_c. From Ref. [7], we infer $z_c = 1.24\omega_0/\sqrt{Q\,|\alpha|}$ assuming nonlinear damping to be negligible. Here, α is the effective nonlinear coefficient (see next section) that can be extracted from the backbone function connecting all resonance peaks at different driving amplitudes. From Ref. [7], we have

$$\omega_{max} - \omega_0 = \frac{3}{8}\frac{\alpha z_0^2}{\omega_0}, \tag{S18}$$

where $\omega_{max}/2\pi$ is the frequency where the amplitude is largest and $\omega_0/2\pi$ is the resonance frequency in the linear regime. In Fig. 1(d) of the main text, we have $\omega_{max} = 2\pi \cdot 46.85\,\mathrm{MHz}$, $\omega_0 = 2\pi \cdot 46.35\,\mathrm{MHz}$, $z_0 = 8.7\,\mathrm{nm}$, and thus get $\alpha = 3.2 \cdot 10^{31}\,\mathrm{m^{-2}s^{-2}}$. Using $Q = 230$ extracted from the resonance width in Fig. 1(c) of the main text, this leads to a critical amplitude of $z_c = 4.2\,\mathrm{nm}$, which is consistent with $z_0 = 3.2\,\mathrm{nm}$ in Fig. 1(c) (where the resonance displays no hysteresis) and with $z_0 = 8.7\,\mathrm{nm}$ in Fig. 1(d) (where there is hysteresis). We repeat the same procedure for the data in Fig. 1(f) of the main text. Here, $\omega_{max} = 2\pi \cdot 123.5\,\mathrm{MHz}$, $\omega_0 = 2\pi \cdot 124.25\,\mathrm{MHz}$, $z_0 = 2.1\,\mathrm{nm}$, and we get $\alpha = -2.2 \cdot 10^{33}\,\mathrm{m^{-2}s^{-2}}$. With $Q = 354$, we calculate $z_c = 1.1\,\mathrm{nm}$, which again is consistent with the results in Fig. 1(e) and (f) (where $z_0 = 0.9\,\mathrm{nm}$ and $2.1\,\mathrm{nm}$, respectively).

XI. STATIC DISPLACEMENT

The reversal of the asymmetry of the resonance between Fig. 1(d) and (f) of the main text is due to a sign change of the effective nonlinearity α [7, 12] which depends on the quadratic and cubic coefficients in Eq. S8 as [6]

$$\alpha = \alpha_3 - \frac{10}{9}\omega_0^{-2}\alpha_2^2. \tag{S19}$$

A comparison of Eq. S6 and Eq. S8 reveals that

$$\alpha_2 = \frac{3E}{4\rho} z_s \left(\frac{\pi}{L}\right)^4 \tag{S20}$$

and

$$\alpha_3 = \frac{E}{4\rho} \left(\frac{\pi}{L}\right)^4. \tag{S21}$$

The asymmetry of the resonance can be used to estimate the static displacement z_s of the resonator at different values of V_g. With α known from the estimations in the last section, we can insert Eq. S20 and Eq. S21 into Eq. S19 in order to obtain z_s. With $E = 1\,\mathrm{TPa}$, $\rho = 2300\,\mathrm{kgm}^{-3}$, and $L = 1.77\,\mu\mathrm{m}$, we get $z_s = 2.8\,\mathrm{nm}$ for $V_g = 1.5\,\mathrm{V}$, and $z_s = 13\,\mathrm{nm}$ for $V_g = 4\,\mathrm{V}$.

XII. ELECTROSTATIC NONLINEARITIES

In the previous sections, we have shown that the sign change of the effective nonlinearity α (from a positive to a negative value) as a function of V_g is consistent with the expected increase of the quadratic nonlinearity α_2. A negative α could also have an electrostatic origin [7, 12]. The quadratic and cubic nonlinearities are $\alpha_2^{el} = -\frac{1}{2m}C'''V_g^2$ and $\alpha_3^{el} = -\frac{1}{2m}C''''V_g^2$, where m is the effective mass of the resonator and C''' and C'''' are the third and fourth derivatives of the capacitance with respect to displacement. The values calculated for $V_g = 4\,\mathrm{V}$ are $\alpha_2^{el} = -4.4 \cdot 10^{22}\,\mathrm{m}^{-1}\mathrm{s}^{-2}$ and $\alpha_3^{el} = -4.0 \cdot 10^{29}\,\mathrm{m}^{-2}\mathrm{s}^{-2}$, which are at least 3 orders of magnitude smaller than the mechanical nonlinearities above. We therefore neglect electrostatic nonlinearities in the analysis of our experiment.

XIII. RESONANCE LINESHAPES

In Fig. 4 of the main manuscript, we show resonance lineshapes with exotic features that we associate with mechanical coupling between commensurate modes of the nanotube. Here, we show how these features vanish and how a usual Duffing nonlinearity is recovered when we reduce the

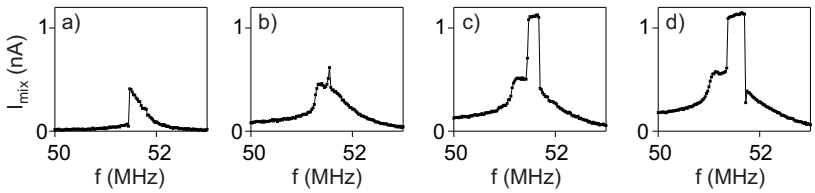

FIG. S7: Resonance lineshape for different driving forces. The resonance is measured with the two-source method for $V_g = 1.88\,\mathrm{V}$ and $V_s^{ac} = 0.28\,\mathrm{mV}$. $V^{ac} = 0.56\,\mathrm{mV}$ in (a), $V^{ac} = 2.2\,\mathrm{mV}$ in (b), $V^{ac} = 3.4\,\mathrm{mV}$ in (c), and $V^{ac} = 4.5\,\mathrm{mV}$ in (d). A conventional Duffing nonlinearity (with $\alpha < 0$) is recovered at the lowest driving force. Sweeps are performed with decreasing frequency.

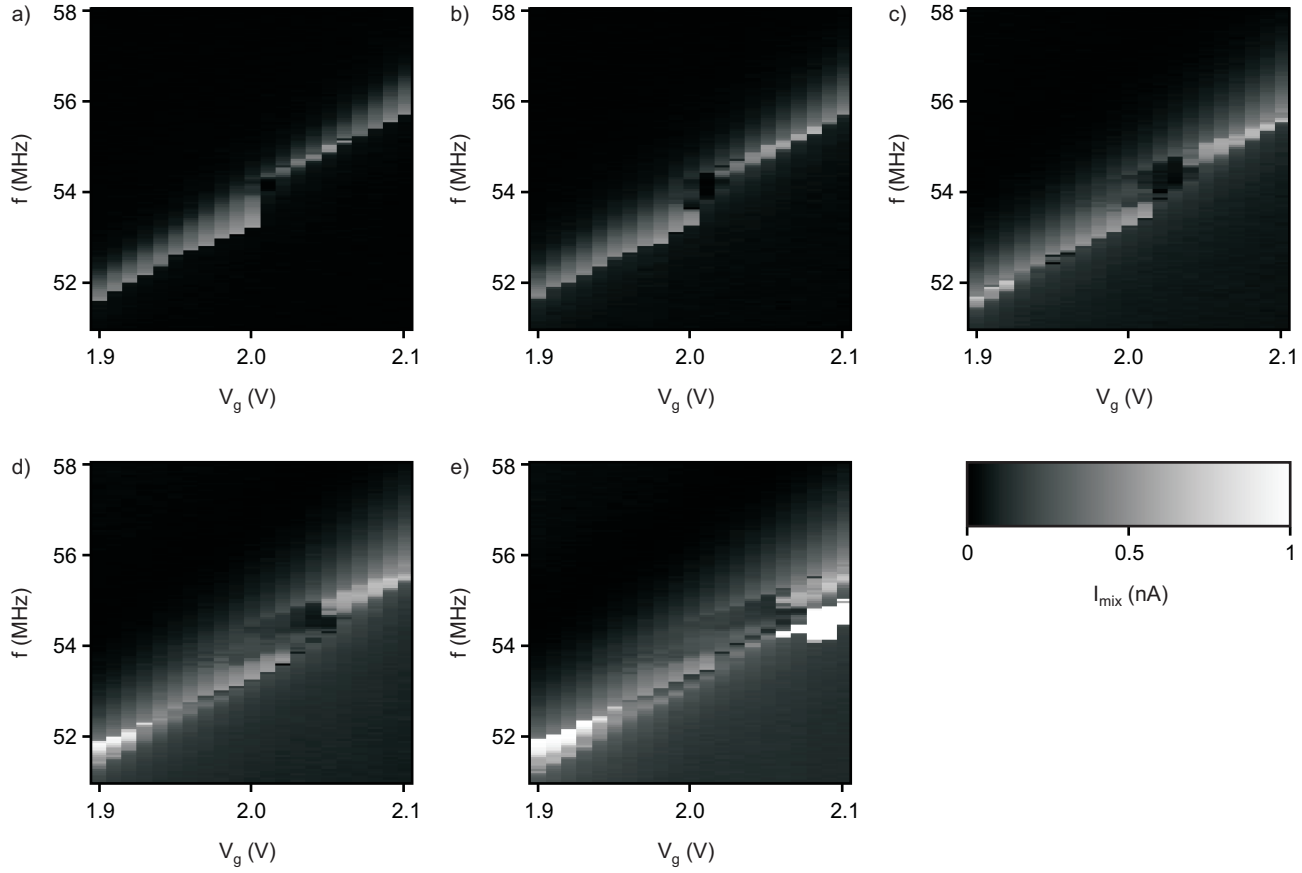

FIG. S8: Mixing current as a function of f and V_g for different driving forces. I_{mix} is measured with the two-source technique with $V_s^{ac} = 0.28\,\mathrm{mV}$. $V^{ac} = 0.56\,\mathrm{mV}$ in (a), $V^{ac} = 1.1\,\mathrm{mV}$ in (b), $V^{ac} = 2.2\,\mathrm{mV}$ in (c), $V^{ac} = 3.4\,\mathrm{mV}$ in (d), and $V^{ac} = 4.5\,\mathrm{mV}$ in (e). Sweeps are performed with decreasing frequency. Panel (b) corresponds to Fig. 4(f) of the main text.

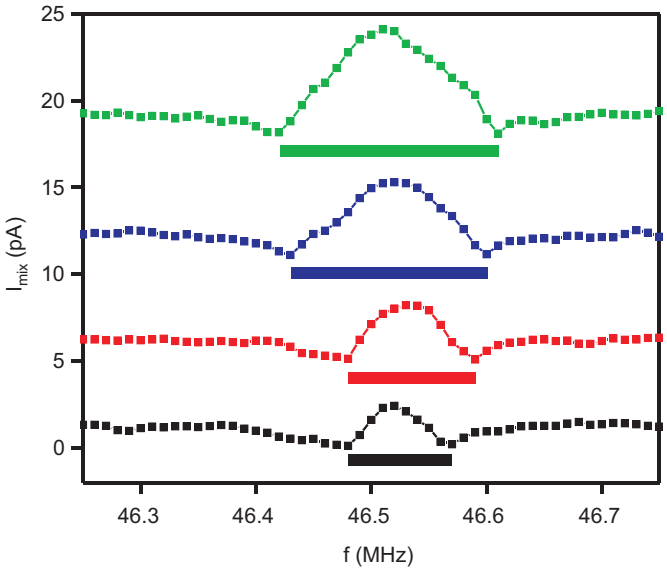

FIG. S9: Increase of the resonance width with V^{ac}. We measure the resonance of mode N at $V_g = 1.5\,\mathrm{V}$ with the FM technique for $V^{ac} = 0.1\,\mathrm{mV}$ (black), $V^{ac} = 0.12\,\mathrm{mV}$ (red), $V^{ac} = 0.15\,\mathrm{mV}$ (blue), and $V^{ac} = 0.2\,\mathrm{mV}$ (green). The distance between the two minima flanking the resonance peak (solid bars) corresponds to the resonance width $\Delta f = f_0/Q$.

driving force. The different panels in Fig. S7 correspond to the same resonance for different driving forces ($\propto V^{ac}$).

A second example with increasing driving force is displayed in Fig. S8. Here, we can observe the evolution from an almost unbroken line (resonance frequency versus V_g) in Fig. S8(a) to a highly exotic response with multiple peaks and dips as a function of f in Fig. S8(e).

XIV. NONLINEAR DAMPING

We recently reported that the resonance width $\Delta f = f_0/Q$ of nanotube and graphene mechanical resonators can depend on the driving voltage V^{ac}. We attributed this phenomenon to the nonlinear damping force $\eta z^2 \dot{z}$ [13]. In the present device, the dominant bistability behaviour prevents observing nonlinear damping above $V^{ac} \sim 0.2\,\mathrm{mV}$. Nontheless, we found an increase of the resonance width for $V^{ac} \leq 0.2\,\mathrm{mV}$ (Fig. S9). In this measurement, we use the frequency modulation technique, which produces two characteristic minima flanking the resonance peak. The separation of these minima corresponds to Δf. A clear increase of Δf is seen between $V^{ac} = 0.1\,\mathrm{mV}$ (below

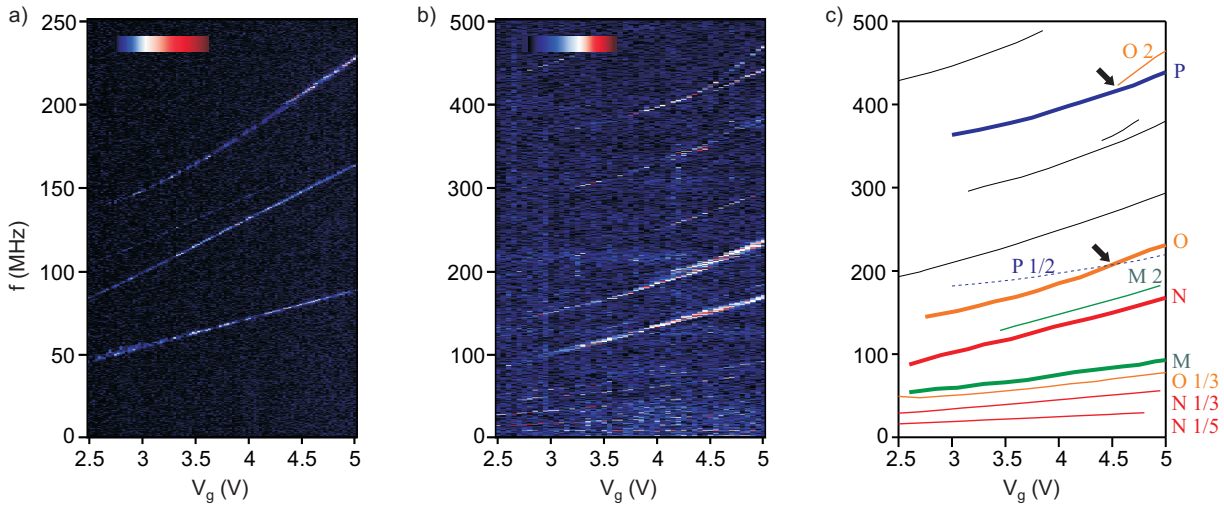

FIG. S10: Map of resonance frequencies as a function of V_g. (a) Frequency modulation measurement at low driving force (obtained by measuring I_{mix} as a function of f and V_g with $V^{ac} = 4\,\mathrm{mV}$). Three resonances are detected with a large signal, a fourth one shows up faintly. Colour scale: 0 (black) to 0.1 nA (dark red). (b) Same measurement with a larger frequency range and $V^{ac} = 40\,\mathrm{mV}$. Colour scale: 0 (black) to 0.1 nA (dark red). (c) Schematic of the map of the resonance frequencies as a function of V_g. Resonances that cannot be assigned to a mode are drawn in black. Black arrows mark regions where modes O and P are commensurate and the resonances lineshapes become exotic.

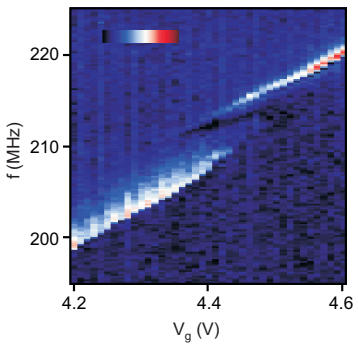

FIG. S11: Modal coupling in the second device. Measurement with the two-source method (obtained by measuring I_{mix} as a function of f and V_g with $V^{ac} = 2.8\,\mathrm{mV}$ and $V_s^{ac} = 0.28\,\mathrm{mV}$). Colour scale: 0 (black) to 0.1 nA (dark red).

this driving voltage the signal vanishes) and $V^{ac} = 0.2\,\mathrm{mV}$.

XV. ADDITIONAL DEVICE

A second nanotube resonator exhibits similar behaviour as the one discussed so far. The results of the second device are summarized in Fig. S10 and Fig. S11. Three modes are clearly visible at low driving force, while a fourth resonance shows up faintly [Fig. S10(a)]. In these measurements, we use the FM technique with $V^{ac} = 4\,\mathrm{mV}$. With a larger driving force ($V^{ac} = 40\,\mathrm{mV}$), many more resonances appear [Fig. S10(b)]. With this device, we have mapped the frequency spectrum up to 500 MHz, and all detected resonances are depicted in Fig. S10(c) and labelled according to the most probable harmonic spectrum. We can identify regions where two modes are commensurate or nearly commensurate and the resonance lineshapes become exotic (black arrows). Around $V_g = 4.4\,\mathrm{V}$, mode P has exactly twice the frequency of mode O (Fig. S11). There, we observe a discontinuity in the map of the resonance frequency as a function of V_g.

[1] J. Cao, Q. Wang, and H. Dai, Nature Mat. **4**, 745 (2005).

[2] A. K. Hüttel, G. A. Steele, B. Witkamp, M. Poot, L. P. Kouwenhoven, and H. S. J. van der Zant, Nano Lett. **9**, 2547 (2009).

[3] G. A. Steele, A. K. Hüttel, B. Witkamp, M. Poot, H. B. Meerwaldt, L. P. Kouwenhoven, and H. S. J. van der Zant, Science **325**, 1103 (2009).

[4] V. Gouttenoire, T. Barois, S. Perisanu, J.-L. Leclercq, S. T. Purcell, P. Vincent, and A. Ayari, Small **6**, 1060 (2010).

[5] V. Sazonova, Y. Yaish, H. Üstünel, D. Roundy, T. A. Arias, and P. L. McEuen, Nature (London) **431**, 284 (2004).

[6] A. H. Nayfeh and D. T. Mook, *Nonlinear Oscillations* (Wiley-VCH, New York, 1979).

[7] R. Lifshitz and M. C. Cross, *Reviews of Nonlinear Dynamics and Complexity* **1** (Wiley-VCH, New York, 2008), available at www.tau.ac.il/ ronlif/pubs/RNDC1-1-2008-preprint.pdf.

[8] A. Eichler, J. Chaste, J., Moser, and A. Bachtold, Nano Lett. **11**, 2699 (2011).

[9] M. I. Dykman, D. G. Luchinsky, R. Mannella, P. V. E. McClintock, S. M. Soskin, and N. D. Stein, Phys. Rev. E **54**, 2366 (1996).

[10] K. N. Kudin, G. E. Scuseria, and B. I. Yakobson, Phys. Rev. B **64**, 235406 (2001).

[11] C. Lee, X. Wei, J. W. Kysar, and J. Hone, Science **321**, 385 (2008).

[12] I. Kozinsky, H. W. Ch. Postma, I. Bargatin, and M. L. Roukes, Appl. Phys. Lett. **88**, 253101 (2006).

[13] A. Eichler, J. Moser, J. Chaste, M. Zdrojek, I. Wilson-Rae, and A. Bachtold, Nature Nanotechnol. **6**, 339 (2011).